Oxygen Redox Activity in Cathodes – a Common Phenomenon Calling for Density-Based Descriptors

Daniel Koch[a] *and Sergei Manzhos*[b]

[a] Department of Mechanical Engineering, National University of Singapore, 9 Engineering Drive 1, Block EA #03-06, Singapore 117576. Email: koch.danielm@gmail.com

[b] Centre Énergie Matériaux Télécommunications, Institut National de la Recherche Scientifique, 1650 boulevard Lionel-Boulet, Varennes QC J3X1S2 Canada. Email: sergei.manzhos@emt.inrs.ca

ABSTRACT: Lithium-excess transition metal oxide materials are promising cathode candidates for future secondary batteries due to their relatively high energy density, which is commonly related to redox-active oxygen centers. First-principle computations are crucial for the understanding of the underlying redox mechanism in these compounds, with plane-wave density functional theory being the most frequently used setup. An important tool for the assignment of the redox-active species is the projected density of states, although the atomic contributions postulated this way do not strictly correspond to any observable physical quantity. By directly analyzing the computed real-space charge density changes, on the other hand, oxygen redox activity can be found to be substantial in most transition metal oxide compounds, although a projection onto atomic states would suggest otherwise. This can be linked to the shortcomings of the commonly employed spherical approximation for ions in crystalline compounds used to compute the projected density of states, which fails to describe the charge density topology in covalent transition metal oxides and leads to a qualitatively different picture from a charge density-based approach, specifically, the underrepresentation of oxygen contributions and exaggeration of transition metal contributions to the density of states The density based approach, due to the non-spherical nature of Bader domains, is more apt to properly describe oxygen redox contributions. This raises the question how meaningful the descriptors of oxygen redox activity are and how it should be acknowledged for transition metal oxide compounds in general.

TOC GRAPHICS

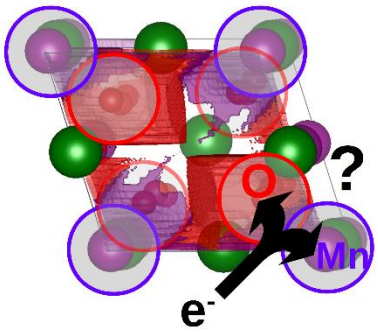

KEYWORDS: Lithium-excess materials, Projected density of states, Oxidation states, Atoms in molecules, Transition metal oxides

Lithium and post-lithium battery cathodes with anionic redox activity during cycling have emerged as heavily investigated material class for future high-performance secondary batteries in recent years. Most of these materials constitute transition metal chalcogenides[1-5] or chalcohalides[6-7] and are primarily of interest due their increased gravimetric capacity compared to the commercially deployed layered transition metal oxides of the O3-type α-$NaFeO_2$ structure (e.g. $LiCoO_2$, $LiNi_xMn_yCo_zO_2$), which is ascribed to the formal oxidation of anions during charge (and conversely a reduction during discharge) providing additional charge storage capability.[8-10] In most of these materials oxide ions (formally O^{2-}) are the anionic species exhibiting this effect and the origin of this redox activity can be briefly summarized as the occupation/de-occupation of O-centered hole states in what can be viewed as heavily p-doped transition metal oxides. While numerous cathode materials with redox-active oxygen centers have emerged since the first reports of this effect,[11-12] Li-excess compounds remain the most intensely investigated representatives, with the eponymous Li excess stemming from the replacement of polyvalent transition metals by monovalent Li in transition metal oxides, introducing multiple O hole states per ion. The prototypical layered Li-excess material Li_2MnO_3 has been discussed in the literature as a model system in order to better understand the O redox mechanism in these compounds theoretically.[8-10, 13] In Figure 1(a) the total and projected (onto the different types of ions) density of states (PDOS) for this material computed with density functional theory (DFT) is shown (see computational details below for more information on the chosen setup). In agreement with previously reported theoretical results,[9] the electronic states at the Fermi level in Li_2MnO_3 are dominated by oxygen contributions, and upon delithiation (oxidation) to $LiMnO_3$ the electron loss in the host material is assigned to the oxide ions. This effect can be also visualized in the charge density difference plot for Li_2MnO_3 in Figure 2(a), where a pronounced electron density

difference on the oxygen centers can be seen. The reason for the unusual preferential redox activity of the oxide over transition metal ions, which, in the case of the corresponding formal Mn^{4+} cations, in principle could still be further oxidized, is the low relative energy of occupied manganese *d* states as shown in Figure 1(a) compared to the oxygen states.[8-10] The situation, however, changes when Mn is replaced with lighter transition metals of the same period, namely Cr or V. The higher energy of transition metal states relative to oxygen leads to increasing hybridization with metal *d* states in Li_2CrO_3 and Li_2VO_3 at the Fermi level and a decreasing importance of oxygen oxidation upon electron loss. While, as shown in Figure 1(b), in Li_2CrO_3 the near-Fermi level states show a mixed transition-metal/oxygen character (similar to what has been reported for the related Li_2MoO_3),[10] the frontier electronic states in Li_2VO_3 exhibit a pronounced transition metal character, shown in Figure 1(c). Hence, the formal reaction mechanism would shift from anionic to cationic redox when going from Li_2MnO_3 over Li_2CrO_3 to Li_2VO_3.

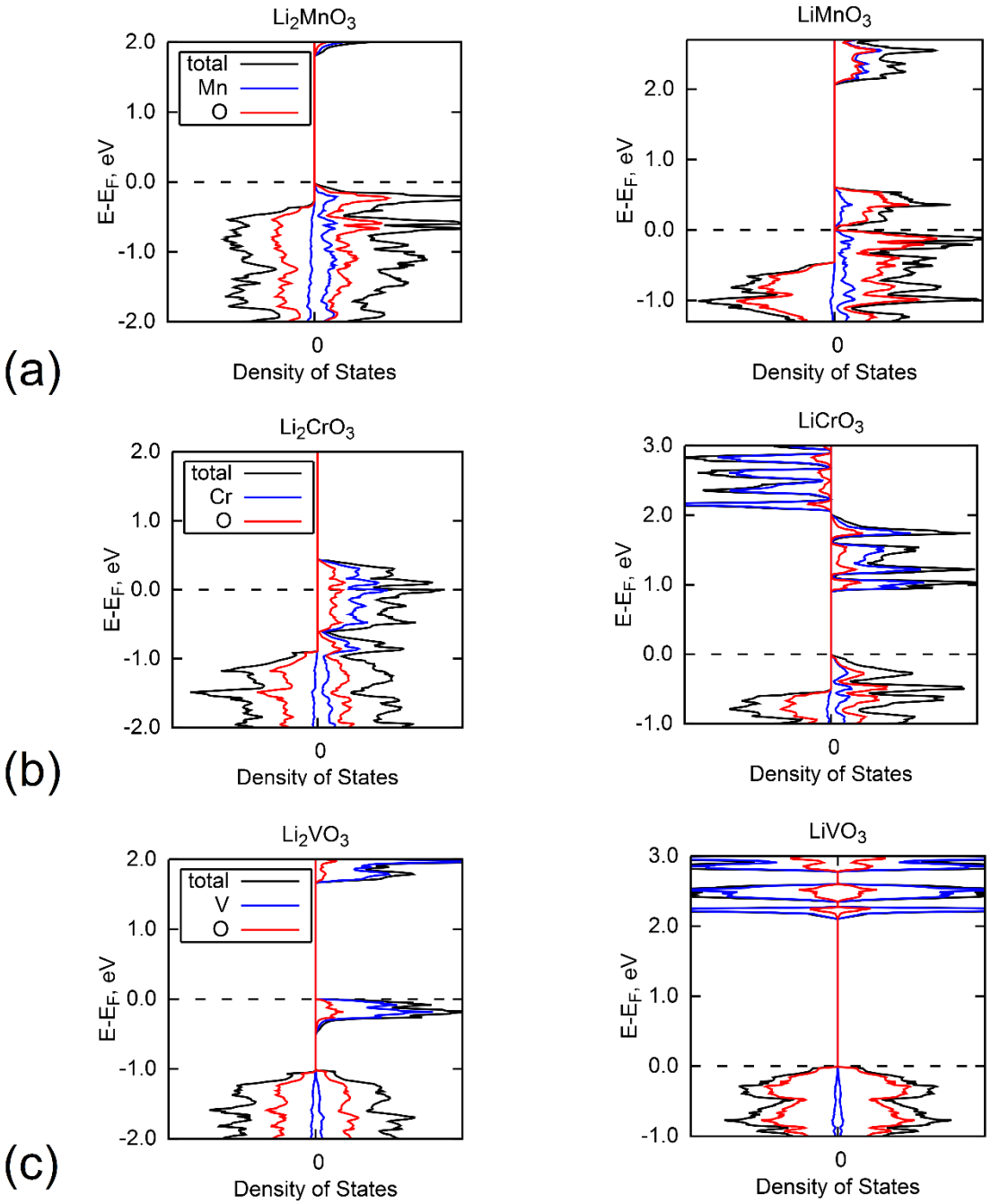

Figure 1. Total (black) and species-projected (transition metals in blue, oxygen in red) densities of states of Li_2MnO_3/$LiMnO_3$ (a), Li_2CrO_3/$LiCrO_3$ (b), and Li_2VO_3/$LiVO_3$ (c). The densities of states for the reduced compounds are shown in the left, the ones for the oxidized ones in the right column, respectively. The energies (E) are relative to the Fermi level (E_F).

Despite the change of the atomic contributions at the Fermi level from oxygen- to transition metal-dominated, the density difference plots in Figure 2 still indicate a significant change in the charge density around the oxygen centers upon removal of Li from Li_2CrO_3 and Li_2VO_3. While the isosurface plots also show a change in electron density around the transition metal centers in these compounds, most of it can be accounted for by a change in *d* orbital magnetic quantum number rather than a loss of charge. Quantitatively, the Bader charges listed in Table 1 show an electron loss of ~0.15 |*e*| per V center when oxidizing Li_2VO_3 to $LiVO_3$, ~0.03 |*e*| per Cr from Li_2CrO_3 to $LiCrO_3$, and an electron gain of ~0.08 |*e*| from Li_2MnO_3 to $LiMnO_3$, while the oxygen centers lose ~0.25 |*e*|, ~0.29 |*e*|, and ~0.32 |*e*| per ion, respectively, and hence account for most of the electron donation in each case. Due to the pronounced covalent character of the transition metal-oxygen bonds, the atomic charges of the transition metal ions obtained from the Bader analysis are significantly lower than what would be expected from their formal oxidation states (FOS). This is consistent with previous theoretical reports which also show that this is not an error of the Bader partitioning itself, but is clearly caused by a valence charge accumulation around the transition metal ions.[14-15] Oxygen contributions to the redox activity are also consistent with the well-established mechanism of charge self-regulation on transition metal centers whereby changes in valence change are smaller than changes in the FOS.[16]

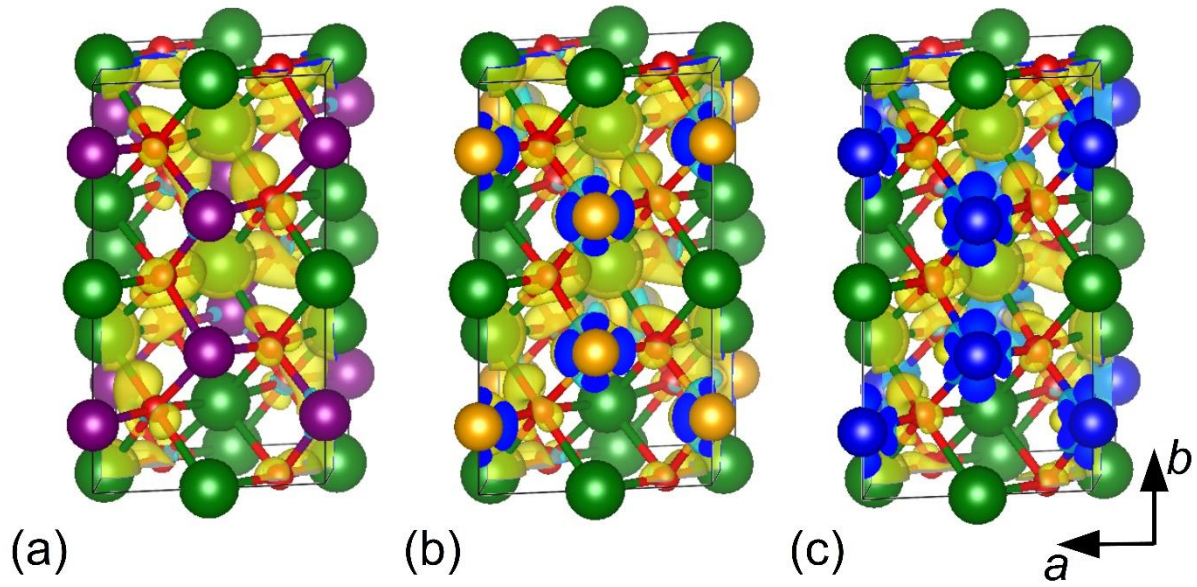

Figure 2. Charge density difference between Li_2MnO_3 and $LiMnO_3$ (a), Li_2CrO_3 and $LiCrO_3$ (b), as well as Li_2VO_3 and $LiVO_3$ (a). Positive density differences are indicated by yellow isosurfaces, negative ones by light blue ones; the isovalue was set to 0.01 e/Å^3. Li atoms are represented by green, Mn by purple, Cr by orange, V by blue, and O by red spheres.

The reason for the oxygen contributions to redox activity being reflected differently in the PDOS and the Bader charge analysis lies in the way these measures are computed: Bader charges rely on the topological partitioning of the electron density in real space (for details see e.g. Ref. 17-19), while the PDOS on the other hand relies on a partitioning of one-electron states between the atomic contributions to this orbital. For computations with localized basis sets the latter can be done in a straightforward manner via a Mulliken-type population analysis using the overlap matrix of the atom-centered basis functions, their LCAO coefficients, and the orbital occupations. The known drawbacks of the Mulliken analysis, like the arbitrarily set equal distribution of the overlap population among the atoms or its basis set dependence, can result in misrepresentations of atomic contributions to the PDOS. While such issues are important to keep in mind for DFT computations in the solid state with atom-centered basis codes like *SIESTA*[20] or

CRYSTAL,[21] the bulk of theoretical literature, including this work, utilizes computations with plane-wave basis sets. Due to the lack of an atomic basis in these codes, some type of projection onto the atomic sites is necessary to decompose the density of states into site and orbital contributions. A frequently used solid state DFT setup are plane-wave basis sets in combination with the projector-augmented wave (PAW) method[22-23] as implemented in the *Vienna Ab Initio Simulation Package* (*VASP*; also employed here, see computational details below).[24] To compute the PDOS, individual states n at point $\mathbf{k}$ in reciprocal space, $|\varphi_{n\mathbf{k}}\rangle$, with occupation $f_{n\mathbf{k}}$ are projected onto spherical harmonics Y_{lm} confined within a sphere around the nuclei. A commonly chosen default setting is to use the radius of the PAW augmentation spheres to define the spherical region. The projection also allows a decomposition into populations ρ by atomic center α and angular momentum l averaged over the number of k points $N_{\mathbf{k}}$ via Equation (1).[25-26]

$$\rho_{\alpha l} = \frac{1}{N_{\mathbf{k}}} \sum_{n\mathbf{k}} f_{n\mathbf{k}} \sum_{m=-l}^{l} |\langle Y_{lm}^{\alpha} | \varphi_{n\mathbf{k}} \rangle|^2 \tag{1}$$

Atomic partial charges q_{partial} can be obtained by subtraction of the atomic populations in Equation (1) from the number of electrons of the respective atom Z via Equation (2) (due to the PAW scheme the number of electrons explicitly taken into account can vary from the nuclear charge).

$$q_{\text{partial}}(\alpha) = Z_{\alpha} - \sum_{l} \rho_{\alpha l} \tag{2}$$

The average partial charges of the transition metal species and oxide ions in the Li-excess compounds discussed above are listed in Table 1 using the default PAW augmentation sphere radii for the projection. Since Li was found to be almost fully ionized in all compounds and

independent of the employed charge analysis method, with only minor variations, it is not discussed explicitly in the following. It should be noted that the total charge which is obtained by projection within the augmentation spheres does not correspond to the number of electrons in the unit cell, but for the compounds in Table 1 only amounts to roughly ~80-85 % of the valence charge, indicating a significant charge remainder in the bonding region outside the augmentation spheres. This leads to the counter-intuitive situation of *positively* charged oxide ions, indicating a significant underestimation of the oxygen contributions compared to the topological charge analysis (an underestimation of the oxygen population by ~30 % on average), while the transition metal partial charges are in better agreement with their Bader charge counterparts (roughly ~5 % average deviation in population). While this is a known drawback of the projection approach and improved algorithms providing more accurate partial charges and DOS have already been proposed,[27-28] it has implications for the qualitative accuracy of the PDOS in VASP, still a commonly used tool to assign which species undergoes oxidation or reduction. The underrepresentation of oxygen contributions, especially in the diffuse region further away from the nucleus and high in energy (close to the Fermi level), important in anionic species, directly translates into an exaggeration of transition metal contributions to the density of states. This is in part caused by an underestimation of the Wigner-Seitz radius of the ions, which leads to consistently smaller volume fractions of oxygen compared to the Bader volumes where the ionic volume per oxygen center exceeds the one of the transition metal by more than 50%; also, the lack of constraint on the shape of the Bader volume allows for a more accurate partitioning even if the average atomic volumes are similar. The fixed default volume ratio between oxygen and transition metal center when using the PAW augmentation sphere volumes (1:4.2 for Mn and Cr,

1:3.3 for V) without regard to the actual ionic species involved further skews the decomposition by atomic site towards the transition metal.

Table 1. Net Bader charges q_{Bader}, net projected partial charges $q_{partial}$, atomic Bader volumes V_{Bader}, and augmentation sphere volumes V_{aug} averaged (where necessary) over the transition metal species (TM) and the oxide ions in the Li-excess materials Li_2MnO_3, Li_2CrO_3, Li_2VO_3, and their oxidized counterparts $LiMnO_3$, $LiCrO_3$, $LiVO_3$. The total cell volumes per formula unit (f. u.) are given for comparison.

	Li_2MnO_3	**$LiMnO_3$**	**Li_2CrO_3**	**$LiCrO_3$**	**Li_2VO_3**	**$LiVO_3$**
q_{Bader}**(TM) [|e|]**	1.778	1.702	1.823	1.850	2.044	2.192
q_{Bader}**(O) [|e|]**	-1.186	-0.866	-1.202	-0.912	-1.277	-1.030
$q_{partial}$**(TM) [|e|]**	1.382	1.322	1.228	0.997	1.562	1.437
$q_{partial}$**(O) [|e|]**	0.974	1.052	0.972	1.01	0.953	0.986
V_{Bader}**(TM) [Å^3]**	7.484	8.725	7.680	8.820	7.619	7.213
V_{Bader}**(O) [Å^3]**	12.680	13.617	12.823	14.271	13.260	14.543
V_{aug}**(TM) [Å^3]**	9.700		9.700		7.550	
V_{aug}**(O) [Å^3]**	2.310					
V_{cell} **/ f.u. [Å^3]**	51.43	52.69	52.09	55.10	53.44	54.05

Generally, the atomic volumes in a cell should roughly add up to the volume of the simulation cell to provide a qualitatively correct PDOS.[25] Using spheres with the same volume as obtained from the Bader analysis for each atom in the cell leads to the correct total volume in which the projection is carried out, but the corresponding radii of ~1.2 Å for the transition metal and ~1.5 Å for O in comparison to metal-oxygen distances below 2.0 Å in all considered structures suggest a significant overlap of the spheres in the bonding region and charge spill-over between

the atomic domains which influence the composition of the PDOS. If the minimum extension of the basins is used instead, better corresponding to a hard sphere-type approximation and minimizing overlap, the resulting atomic radii of ~0.8-0.9 Å for the transition metals and oxygen alike again lead to a severe underestimation of the total population (only about ~75% of the simulation cell charge), leaving out crucial anionic charge density components at large distances from the oxygen nuclei. Both approaches, while mildly changing the transition metal-oxygen ratio of the PDOS at the Fermi level, do not reproduce the significant oxygen contribution to redox activity found from Bader charges in Li_2CrO_3/$LiCrO_3$ and Li_2VO_3/$LiVO_3$. The disparity between Bader analysis and PDOS is hence not trivially resolved by an adjustment of the spherical domains in which the projection is performed, but a result of the non-spherical nature of the Bader domains, which are shown in Figure 3 on the example of Li_2MnO_3. The hybridization of *s* and *p* valence states results in a rather convex oxygen Bader volume shape, while the *d* dominated transition metal density gives rise to a concavely shaped domain. The spherical approximation of the latter hence might lead to a substantial cut beyond the inward-bent faces for sphere radii larger than the minimum extent of the Bader domain, ascribing crucial oxygen contributions to the transition metal, while the spherical approximation for oxygen would rather tend to disregard the outer perimeter of the Bader volume.

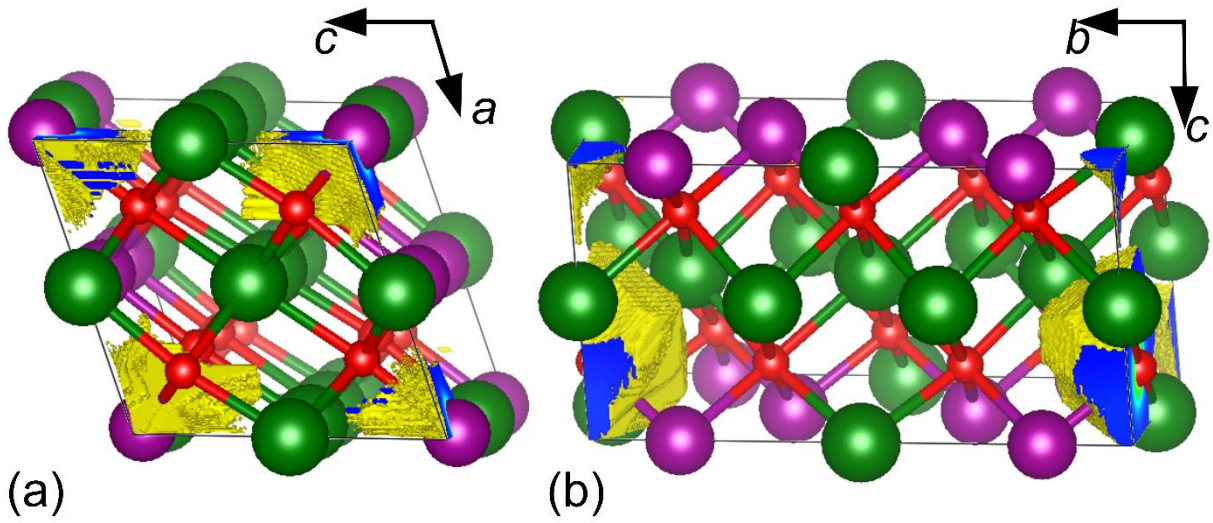

Figure 3. Shape of the Bader volumes of the transition metal (a) and oxygen (b) in Li_2MnO_3. The Bader volume is shown in yellow (surface) or blue (cuts), while manganese, oxygen and lithium centers are represented by purple, red, and green spheres, respectively.

Experimental investigations on oxygen redox activity reported in the literature rely on techniques like e.g. electron energy loss spectroscopy (EELS)[29] or X-ray absorption spectroscopy (XAS),[4, 7] but it should be noted that the interpretation of these results is based on the comparison with reference compounds and they do not provide an unambiguous way to determine atomic charge states in molecules or bulk. Due to the covalent character of bonding in "ionic" transition metal compounds, such benchmarks themselves do not provide pure metal ion reference states. Analyzing (the somewhat artificial concept of) atomic orbital contributions is only possible in *ab initio* computations, since these are not physical observables themselves. The electron densities, however, are observables and their changes in principle measurable, which is an argument in support of topological charge partitioning schemes like the Bader analysis.[14, 30] The latter shows a substantial oxygen redox activity in all three model compounds, independent of the computed PDOS character at the Fermi level due to the reasons described above. The

origin of this oxygen redox activity becomes apparent when comparing the transition metal charge states in the Li-excess compounds to those of the pure transition metal oxides with various FOS of the metals as shown in Figure 4: the metal charges approach a maximum value with increasing oxygen content (FOS of the metal) which ranges between ~+1.8 |*e*| and ~+2.3 |*e*|, depending on the transition metal (see computational details below for a list of the transition metal oxide structures included). These charges significantly differ from the FOS of the transition metals due to the pronounced covalency of the transition metal-oxygen bonds in agreement with previous theoretical and experimental findings (while for main group metals the FOS roughly corresponds to the real-space charge state).[14, 16, 31-33] The computed trends are consistent with what we previously reported for transition metal aquo complexes, where similar charge loss limits of the transition metals were found, which enabled us to propose a Bader charge-based explanation for the formation of oxo an- and cations of transition metals in aqueous solution [34].

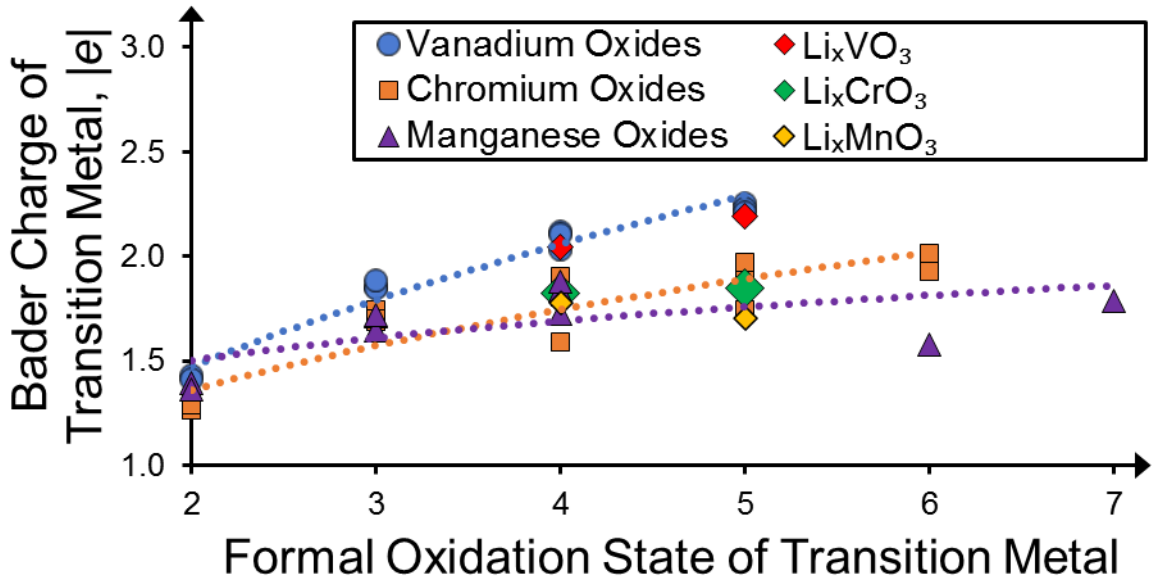

Figure 4. Computed Bader charges for different vanadium (blue circles), chromium (orange squares), and manganese oxides (purple triangles) in dependence on their formal oxidation state. The Bader charges for the Li-excess compounds $LiVO_3/Li_2VO_3$ (red diamonds), $LiCrO_3/Li_2CrO_3$ (green diamonds), and $LiMnO_3/Li_2MnO_3$ (yellow diamonds) are also included for comparison. Least-squares fit power functions (dotted lines) are included for a better visibility of the trends.

As can be seen in Figure 4, vanadium oxides are the most ionic compounds with the greatest variability of charge states, followed by the less ionic chromium oxides, and the most covalent manganese oxides. As a rule of thumb, the cationic charges in vanadium and chromium oxides roughly correspond to $\sim(FOS)^{1/2}$ and $\sim(FOS)^{1/3}$, respectively, while in manganese oxides they first scale similar to chromium oxides, but again slightly drop at higher oxygen content. The differing slopes are related to the increasing valence electron binding strength within a row in the periodic table[35] and the resulting energetically lower-lying transition metal *d* electrons incapable of abstraction by oxygen. The transition metal charge states in the Li-excess compounds discussed above are similar to the ones in the corresponding oxides with the same FOS of the transition metal. The more pronounced oxygen redox activity in Li_2MnO_3 can hence be

explained by the reluctance of (formal) Mn^{4+} centers to oxidation, although the redox activity of transition metals is generally low and commonly exaggerated relative to their actual real-space charge losses and gains. This is by no means restricted to Li-excess cathode materials as a comparison with α-V_2O_5 (space group *Pmmn*) shows, a regularly investigated candidate material for future high-performance Li ion battery cathodes.[36-38] For the lithiation of this material to α-LiV_2O_5 the PDOS shown in Figure 5(a) and (b) suggest an electron donation to an almost pure vanadium state. However, the calculated electron density difference in Figure 5(c) shows a non-negligible change in the density around oxygen, while changes around vanadium are again mostly due to a change in orbital shape. Quantitatively, the Bader charge analysis supports the latter observation, assigning ~0.70 |*e*| of the ~0.93 |*e*| donated by each Li atom to oxygen centers and only ~0.23 |*e*| to vanadium.

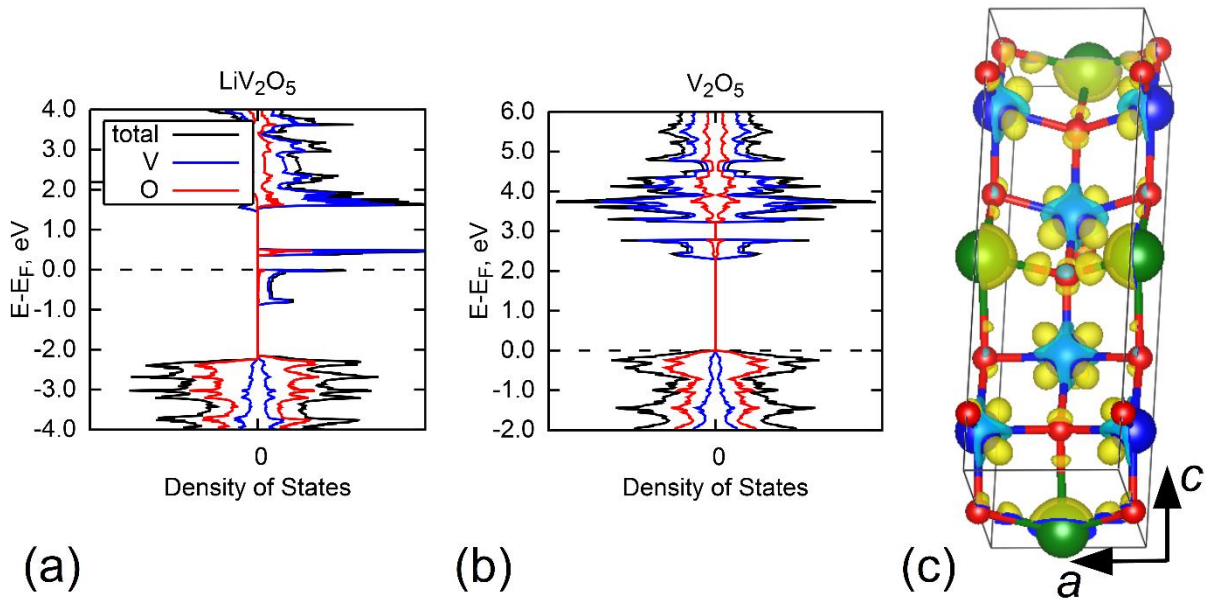

Figure 5. Total and projected densities of states of lithiated (a), and pristine (b) α-V_2O_5 (vanadium plotted in blue, oxygen in red, total in black) as well as the corresponding charge density difference between the two (c). The energies (*E*) are relative to the Fermi level (E_F). Positive density differences are indicated by yellow isosurfaces, negative ones by light blue ones; the isovalue was set to 0.008 e/Å^3. Li atoms are represented by green, V by blue, and O by red spheres.

To summarize, we find significant charge density changes around oxygen in the prototypical Li-excess material Li_2MnO_3 upon oxidation to $LiMnO_3$, but also for its Cr and V counterparts, which would not be expected from the composition of the PDOS of the latter two near the Fermi level. We can relate this to an incomplete projection of O-near density caused by its small augmentation sphere, resulting in an exaggerated transition metal contribution to the valence band maximum. We generally find a low variability of transition metal charge states in their respective oxides, suggesting that any oxidation or reduction of these compounds is mostly carried by charge density changes around oxygen, in agreement with previous theoretical studies.[16, 31, 33-34, 39] While we indeed find a more pronounced oxygen redox activity in the prototypical Li-excess material Li_2MnO_3, its rather small difference compared to oxides with what is formally classified as conventional transition metal redox activity raises the question whether such a classification is actually justified, or whether it should be rather expanded to all transition metal oxide compounds in general.

Computational Details

All computations were performed with the exchange-correlation functional of Perdew, Burke, and Ernzerhof (PBE)[40-41] as implemented in the program package VASP 5.4.4[24] using a plane wave basis and the projector-augmented wave method.[22-23] An energy-converged plane-wave cutoff of 600 eV was chosen with a gamma-centered k-point grid with at least 36 points·Å in each dimension[42] and a SCF convergence threshold of 10^{-4} eV. The real-space grid for charge density integration was set to 27,000 points/Å^3. Geometry optimizations were performed on all structures with a conjugate gradient algorithm until force convergence below 0.02 eV/Å was reached. The tetrahedron method with Blöchl corrections was used for Brillouin zone

integrations,[43] and a grid-based Bader analysis performed with the BADER code version 0.95a.[30, 44-46] The rotationally invariant LSDA+*U* correction proposed by Dudarev *et al*.[47] was applied on transition metal *d* states with empirically tuned *U* parameters of 3.10 eV (V), 3.50 eV (Cr), and 4.0 eV (Mn) reported in literature.[48] Li_2MO_3 cells (*M* = V, Cr, Mn) with space group *C2/m* containing four formula units were employed for the simulations. Interlayer Li atoms with largest mutual distance were removed to generate $LiMO_3$ structures which were subsequently fully relaxed for the comparison of Bader charges and volumes as well as partial charges and projected densities of states. Density differences were computed by subtracting the charge density of the Li_2MO_3 cells from the ones of the corresponding $LiMO_3$ with one interlayer Li atom per formula unit removed, but without an additional structure relaxation.

There exists some ambiguity with regard to the computational setup used, which utilizes an exchange-correlation functional of the generalized gradient approximation-type with a Hubbard correction applied on transition metal *d* states and an empirically tuned *U* parameter. It is known that the PDOS composition at the Fermi level as well as the real-space charge distribution is sensitive to the magnitude of the *U* parameter,[10] which generally lowers the energy of *d* states and causes electron localization on transition metal centers. For this reason, hybrid functionals are sometimes employed for quantitatively more accurate results.[9] However, these come at a high computational cost which in this specific case is not justified, as the purpose of the above discussion is to give a qualitative comparison between real-space charge distributions for different types of PDOS state orderings with the commonly use plane-wave/PAW DFT approach, which is not dependent on the functional type used.

The different transition metal oxide starting structures were obtained from the *Materials Project* database.[49] The selected structures were: *P6₃mc* and *Fm-3m* MnO; *Pbca*, *R-3c*, and *Ia-3*

Mn_2O_3; *C2/m*, *P4₂/m*, and *I4/m* MnO_2; *Imma* MnO_3; *P2₁/c* Mn_2O_7; *C2/c*, *P4₂/mmc*, and *Fm-3m* CrO; *Pbcn*, *R-3*, and *R-3c* Cr_2O_3; *C2/m*, *Pnma*, and *P4₂/mnm* CrO_2; *P2₁2₁2₁*, *Pbam*, and *Pmmn* Cr_2O_5; *Ama2*, *P6₃mmc*, and *Pm-3m* CrO_3; *R-3m* and *Fm-3m* VO; *C2/c*, *R-3c*, and *Ia-3* V_2O_3; *C2/m*, *P2₁/c*, and *P4₂/mnm* VO_2; *P2₁/m*, *C2/c*, and *Pmmn* V_2O_5. The structures were relaxed, all computations were performed with the computational setup described above.

References

(1) Kang, S. H.; Johnson, C. S.; Vaughey, J. T.; Amine, K.; Thackeray, M. M. The Effects of Acid Treatment on the Electrochemical Properties of 0.5 $Li_2MnO_3 \cdot 0.5\ LiNi_{0.44}Co_{0.25}Mn_{0.31}O_2$ Electrodes in Lithium Cells. *J. Electrochem. Soc.* **2006**, *153* (6), A1186.

(2) Lu, Z.; MacNeil, D. D.; Dahn, J. R. Layered Cathode Materials $Li[Ni_xLi_{(1/3-2x/3)}Mn_{(2/3-X/3)}]O_2$ for Lithium-Ion Batteries. *Electrochem. Solid-State Lett.* **2001**, *4* (11), A191.

(3) Pearce, P. E.; Perez, A. J.; Rousse, G.; Saubanère, M.; Batuk, D.; Foix, D.; McCalla, E.; Abakumov, A. M.; Van Tendeloo, G.; Doublet, M.-L.; Tarascon, J.-M. Evidence for Anionic Redox Activity in a Tridimensional-Ordered Li-Rich Positive Electrode B-Li_2iro_3. *Nat. Mater.* **2017**, *16* (5), 580-586.

(4) Shadike, Z.; Zhou, Y.-N.; Chen, L.-L.; Wu, Q.; Yue, J.-L.; Zhang, N.; Yang, X.-Q.; Gu, L.; Liu, X.-S.; Shi, S.-Q.; Fu, Z.-W. Antisite Occupation Induced Single Anionic Redox Chemistry and Structural Stabilization of Layered Sodium Chromium Sulfide. *Nat. Commun.* **2017**, *8* (1), 566.

(5) Yabuuchi, N.; Takeuchi, M.; Nakayama, M.; Shiiba, H.; Ogawa, M.; Nakayama, K.; Ohta, T.; Endo, D.; Ozaki, T.; Inamasu, T.; Sato, K.; Komaba, S. High-Capacity Electrode Materials for Rechargeable Lithium Batteries: Li_3nbo_4-Based System with Cation-Disordered Rocksalt Structure. *Proc. Natl. Acad. Sci. USA* **2015**, *112* (25), 7650.

(6) Clément, R. J.; Lun, Z.; Ceder, G. Cation-Disordered Rocksalt Transition Metal Oxides and Oxyfluorides for High Energy Lithium-Ion Cathodes. *Energy Environ. Sci.* **2020**, *13* (2), 345-373.

(7) House, R. A.; Jin, L.; Maitra, U.; Tsuruta, K.; Somerville, J. W.; Förstermann, D. P.; Massel, F.; Duda, L.; Roberts, M. R.; Bruce, P. G. Lithium Manganese Oxyfluoride as a New Cathode Material Exhibiting Oxygen Redox. *Energy Environ. Sci.* **2018**, *11* (4), 926-932.

(8) Saubanère, M.; McCalla, E.; Tarascon, J. M.; Doublet, M. L. The Intriguing Question of Anionic Redox in High-Energy Density Cathodes for Li-Ion Batteries. *Energy Environ. Sci.* **2016**, *9* (3), 984-991.

(9) Seo, D.-H.; Lee, J.; Urban, A.; Malik, R.; Kang, S.; Ceder, G. The Structural and Chemical Origin of the Oxygen Redox Activity in Layered and Cation-Disordered Li-Excess Cathode Materials. *Nat. Chem.* **2016**, *8* (7), 692-697.

(10) Xie, Y.; Saubanère, M.; Doublet, M. L. Requirements for Reversible Extra-Capacity in Li-Rich Layered Oxides for Li-Ion Batteries. *Energy Environ. Sci.* **2017**, *10* (1), 266-274.

(11) Maitra, U.; House, R. A.; Somerville, J. W.; Tapia-Ruiz, N.; Lozano, J. G.; Guerrini, N.; Hao, R.; Luo, K.; Jin, L.; Pérez-Osorio, M. A.; Massel, F.; Pickup, D. M.; Ramos, S.; Lu, X.; McNally, D. E.; Chadwick, A. V.; Giustino, F.; Schmitt, T.; Duda, L. C.; Roberts, M. R.; Bruce, P. G. Oxygen Redox Chemistry without Excess Alkali-Metal Ions in $Na_{2/3}[Mg_{0.28}Mn_{0.72}]O_2$. *Nat. Chem.* **2018**, *10* (3), 288-295.

(12) Sato, K.; Nakayama, M.; Glushenkov, A. M.; Mukai, T.; Hashimoto, Y.; Yamanaka, K.; Yoshimura, M.; Ohta, T.; Yabuuchi, N. Na-Excess Cation-Disordered Rocksalt Oxide: $Na_{1.3}Nb_{0.3}Mn_{0.4}O_2$. *Chem. Mater.* **2017**, *29* (12), 5043-5047.

(13) Okubo, M.; Yamada, A. Molecular Orbital Principles of Oxygen-Redox Battery Electrodes. *ACS Appl. Mater. Interfaces* **2017**, *9* (42), 36463-36472.

(14) Koch, D.; Manzhos, S. On the Charge State of Titanium in Titanium Dioxide. *J. Phys. Chem. Lett.* **2017**, *8* (7), 1593-1598.

(15) Koch, D.; Manzhos, S. Addition to “on the Charge State of Titanium in Titanium Dioxide”. *J. Phys. Chem. Lett.* **2017**, *8* (17), 3945-3946.

(16) Raebiger, H.; Lany, S.; Zunger, A. Charge Self-Regulation Upon Changing the Oxidation State of Transition Metals in Insulators. *Nature* **2008**, *453* (7196), 763-766.

(17) Bader, R. F. W. A Quantum Theory of Molecular Structure and Its Applications. *Chem. Rev.* **1991**, *91* (5), 893-928.

(18) Bader, R. F. W. The Quantum Mechanical Basis of Conceptual Chemistry. *Monatsh. Chem.* **2005**, *136* (6), 819-854.

(19) Bader, R. F. W. *Atoms in Molecules: A Quantum Theory*. Clarendon Press: 1990.

(20) Soler, J. M.; Artacho, E.; Gale, J. D.; García, A.; Junquera, J.; Ordejón, P.; Sánchez-Portal, D. The Siesta Method for Ab Initio Order-*N* Materials Simulation. *J. Phys.: Condens. Matter* **2002**, *14* (11), 2745-2779.

(21) Dovesi, R.; Erba, A.; Orlando, R.; Zicovich-Wilson, C. M.; Civalleri, B.; Maschio, L.; Rérat, M.; Casassa, S.; Baima, J.; Salustro, S.; Kirtman, B. Quantum-Mechanical Condensed Matter Simulations with Crystal. *Wiley Interdiscip. Rev. Comput. Mol. Sci.* **2018**, *8* (4), e1360.

(22) Blöchl, P. E. Projector Augmented-Wave Method. *Phys. Rev. B* **1994**, *50* (24), 17953-17979.

(23) Kresse, G.; Joubert, D. From Ultrasoft Pseudopotentials to the Projector Augmented-Wave Method. *Phys. Rev. B* **1999**, *59* (3), 1758-1775.

(24) Kresse, G.; Furthmüller, J. Efficient Iterative Schemes for Ab Initio Total-Energy Calculations Using a Plane-Wave Basis Set. *Phys. Rev. B* **1996**, *54* (16), 11169-11186.

(25) Vasp User Manual. URL: https://www.vasp.at/wiki/index.php/LORBIT (accessed 12/05/2020).

(26) Schüler, M.; Peil, O. E.; Kraberger, G. J.; Pordzik, R.; Marsman, M.; Kresse, G.; Wehling, T. O.; Aichhorn, M. Charge Self-Consistent Many-Body Corrections Using Optimized Projected Localized Orbitals. *J. Phys.: Condens. Matter* **2018**, *30* (47), 475901.

(27) Maintz, S.; Deringer, V. L.; Tchougréeff, A. L.; Dronskowski, R. Analytic Projection from Plane-Wave and Paw Wavefunctions and Application to Chemical-Bonding Analysis in Solids. *J. Comput. Chem.* **2013**, *34* (29), 2557-2567.

(28) Maintz, S.; Deringer, V. L.; Tchougréeff, A. L.; Dronskowski, R. Lobster: A Tool to Extract Chemical Bonding from Plane-Wave Based Dft. *J. Comput. Chem.* **2016**, *37* (11), 1030-1035.

(29) Wang, R.; Li, X.; Liu, L.; Lee, J.; Seo, D.-H.; Bo, S.-H.; Urban, A.; Ceder, G. A Disordered Rock-Salt Li-Excess Cathode Material with High Capacity and Substantial Oxygen Redox Activity: $Li_{1.25}Nb_{0.25}Mn_{0.5}O_2$. *Electrochem. Commun.* **2015**, *60*, 70-73.

(30) Tang, W.; Sanville, E.; Henkelman, G. A Grid-Based Bader Analysis Algorithm without Lattice Bias. *J. Phys.: Condens. Matter* **2009**, *21* (8), 084204.

(31) Koch, D.; Golub, P.; Manzhos, S. Stability of Charges in Titanium Compounds and Charge Transfer to Oxygen in Titanium Dioxide. *J. Phys. Conf. Ser.* **2018**, *1136*, 012017.

(32) Wolczanski, P. T. Flipping the Oxidation State Formalism: Charge Distribution in Organometallic Complexes as Reported by Carbon Monoxide. *Organometallics* **2017**, *36* (3), 622-631.

(33) Szymanski, N. J.; Liu, Z. T. Y.; Alderson, T.; Podraza, N. J.; Sarin, P.; Khare, S. V. Electronic and Optical Properties of Vanadium Oxides from First Principles. *Comput. Mater. Sci.* **2018**, *146*, 310-318.

(34) Koch, D.; Manzhos, S. The Role of Solvent Charge Donation in the Stabilization of Metal Ions in Aqueous Solution. *MRS Commun.* **2018**, *8* (3), 1139-1144.

(35) Lang, P. F.; Smith, B. C. Ionization Energies of Atoms and Atomic Ions. *J. Chem. Educ.* **2003**, *80* (8), 938.

(36) Li, Q.; Chen, D.; Tan, H.; Zhang, X.; Rui, X.; Yu, Y. 3d Porous V_2O_5 Architectures for High-Rate Lithium Storage. *J. Energy Chem.* **2020**, *40*, 15-21.

(37) Natarajan, S.; Kim, S.-J.; Aravindan, V. Restricted Lithiation into a Layered V_2o_5 Cathode Towards Building "Rocking-Chair" Type Li-Ion Batteries and Beyond. *Journal of Materials Chemistry A* **2020**, *8* (19), 9483-9495.

(38) Tan, H.; Yu, X. Z.; Huang, K.; Zhong, J.; Lu, B. Large-Scale Carambola-Like V_2O_5 Nanoflowers Arrays on Microporous Reed Carbon as Improved Electrochemical Performances Lithium-Ion Batteries Cathode. *J. Energy Chem.* **2020**, *51*, 388-395.

(39) Wu, L.; Cao, X.-R.; Wu, S.-Q.; Yang, Y.; Zhu, Z.-Z. Ab Initio Calculations on the Electronic Structures and Electrochemical Properties of $LiVO_2$ and $NaVO_2$. *J. Solid State Chem.* **2020**, *288*, 121383.

(40) Perdew, J. P.; Burke, K.; Ernzerhof, M. Generalized Gradient Approximation Made Simple. *Phys. Rev. Lett.* **1996**, *77* (18), 3865-3868.

(41) Perdew, J. P.; Burke, K.; Ernzerhof, M. Generalized Gradient Approximation Made Simple [Phys. Rev. Lett. 77, 3865 (1996)]. *Phys. Rev. Lett.* **1997**, *78* (7), 1396-1396.

(42) Monkhorst, H. J.; Pack, J. D. Special Points for Brillouin-Zone Integrations. *Phys. Rev. B* **1976**, *13* (12), 5188-5192.

(43) Blöchl, P. E.; Jepsen, O.; Andersen, O. K. Improved Tetrahedron Method for Brillouin-Zone Integrations. *Phys. Rev. B* **1994**, *49* (23), 16223-16233.

(44) Henkelman, G.; Arnaldsson, A.; Jónsson, H. A Fast and Robust Algorithm for Bader Decomposition of Charge Density. *Comput. Mater. Sci.* **2006**, *36* (3), 354-360.

(45) Sanville, E.; Kenny, S. D.; Smith, R.; Henkelman, G. Improved Grid-Based Algorithm for Bader Charge Allocation. *J. Comput. Chem.* **2007**, *28* (5), 899-908.

(46) Yu, M.; Trinkle, D. R. Accurate and Efficient Algorithm for Bader Charge Integration. *J. Chem. Phys.* **2011**, *134* (6), 064111.

(47) Dudarev, S. L.; Botton, G. A.; Savrasov, S. Y.; Humphreys, C. J.; Sutton, A. P. Electron-Energy-Loss Spectra and the Structural Stability of Nickel Oxide: An LSDA+U Study. *Phys. Rev. B* **1998**, *57* (3), 1505-1509.

(48) Wang, L.; Maxisch, T.; Ceder, G. Oxidation Energies of Transition Metal Oxides within the GGA+*U* Framework. *Phys. Rev. B* **2006**, *73* (19), 195107.

(49) Jain, A.; Ong, S. P.; Hautier, G.; Chen, W.; Richards, W. D.; Dacek, S.; Cholia, S.; Gunter, D.; Skinner, D.; Ceder, G.; Persson, K. A. Commentary: The Materials Project: A Materials Genome Approach to Accelerating Materials Innovation. *APL Mater.* **2013**, *1* (1), 011002.